Research Article | Vol. 30, No. 26 / 19 Dec 2022 / Optics Express 46294
Optics EXPRESS

Numerical model of light propagation through Fabry-Perot etalons composed of interfaces with non-planar surface topography

DYLAN M. MARQUES,[1,2,*] JAMES A. GUGGENHEIM,[1,2,3] AND PETER R. T. MUNRO[1]

[1]Department of Medical Physics and Biomedical Engineering, University College London, London, UK
[2]Institute of Cardiovascular Sciences, University of Birmingham, Birmingham, UK
[3]School of Computer Science, University of Birmingham, UK
*d.marques@bham.ac.uk

Abstract: We present a model that calculates optical fields reflected and transmitted by a Fabry-Perot (FP) etalon composed of interfaces with non-planar surface topography. The model uses the Rayleigh-Rice theory, which predicts the fields reflected and transmitted by a single interface, to account for the non-planar surface topography of each interface. The Rayleigh-Rice theory is evaluated iteratively to account for all round trips that light can take within the FP etalon. The model predictions can then be used to compute Interferometer transfer function (ITF)s, by performing wavelength or angle resolved simulations enabling predictions of the bandwidth, peak transmissivity, and sensitivity of FP etalons. The model was validated against the Pseudospectral time-domain (PSTD) method, which resulted in good agreement. Since the model accuracy is expected to reduce as the Root mean square (RMS) of the topographic map increases, the error in the model's predictions was studied as a function of topographic map RMS. Finally, application of the model was exemplified by predicting the impact of roughness on ITFs and computing the changes in FP etalon transmissivity as cavity thickness is modulated by an ultrasonic wave.

1. Introduction

A Fabry-Perot (FP) etalon is an optical cavity formed between two mirrors [1] and is mainly used as a wavelength filter [2] or as a sensor [3,4]. If designed with a high Q-factor (i.e. high mirror reflectivity), an FP etalon is reflective throughout most of its spectral range and becomes transparent in a very narrow range where the optical cavity thickness closely matches an integer number of wavelengths. Under this condition, light is in resonance inside the cavity and the wavelength is typically called the resonance wavelength. The rapid change in transmissivity and reflectivity associated with this resonance is commonly used for sensing by designing FP etalons with a cavity thickness modulated by a perturbation (such as an ultrasonic wave). This cavity thickness modulation leads to a shift in the resonance wavelength, thus modulating the reflectivity and transmissivity near the original resonance wavelength [5]. The performance of FP etalons is generally characterised by a wavelength resolved reflectivity or transmissivity measurement, typically called an Interferometer transfer function (ITF). The ITF predicts, for example, the transmission spectral bandwidth, the peak transmissivity and the sensitivity (which is related to the maximum ITF derivative) of an FP etalon.

FP etalons are usually modelled as planar layered structures, i.e., as a succession of planar and parallel layers. Assuming plane wave illumination, FP etalons are simulated using the Airy function which predicts the reflectivity and transmissivity of the FP etalon [6]. However, the Airy function is not valid if the FP etalon is illuminated by a focused beam. In such cases, the

#472308 https://doi.org/10.1364/OE.472308
Journal © 2022 Received 14 Aug 2022; revised 13 Nov 2022; accepted 13 Nov 2022; published 6 Dec 2022

Optics EXPRESS

angular Airy function can be used to compute the reflected and transmitted beams assuming an arbitrary illumination beam [7–9]. Both models simulate the FP etalon solely based on its mirror reflectivities, optical cavity thickness and illumination beam. Alternatively, FP etalons can be simulated based on the dielectric stack forming the FP etalon [10]. In this case, the simulation is performed based on the refractive index and thickness of all layers forming the FP etalon. The latter FP etalon description simulates its physical structure, and thus all optical effects, including the changes in the light phase and absorption, are intrinsically accounted for in the simulations [10].

However, treating the FP etalon as a planar layered structure does not allow for the modelling of small variations in the surface topography of the interfaces between layers, which are often present in FP etalons. For example, when used for sensing, the cavity thickness is typically locally modulated up to a few nanometers by a perturbation, such as an ultrasonic wave or temperature change [11]. Including the modulation of the interfaces' surface topography by the perturbation is important to understand the relationship between the optical beam spot size and the sensing element size. This relation depends on complex physical phenomena including beam divergence inside the cavity, beam wavefront, and the number of round trips that light undergoes inside the cavity. Additionally, the interfaces of FP etalons can have a surface topography exhibiting rough profiles. Studying such rough FP etalons is particularly important for FP etalons with a cavity made of a polymer [12] which might exhibit some degree of roughness [13]. Simulating these FP etalons could quantify the impact of roughness on bandwidth, transmissivity peak, and sensitivity whilst allowing for computing optimal designs and manufacturing tolerances.

To study such examples, a model able to simulate FP etalons made of interfaces with non-planar topography, on the order of a few nanometers, is needed. In principle, models assuming a discretized three-dimensional volume with arbitrary refractive index distribution, such as Finite-difference time-domain (FDTD) [14] or Pseudospectral time-domain (PSTD) [15] methods, can perform these simulations. However, in practice, such models are unsuitable for the current application. This is because sampling three-dimensional space with a sampling period below 1 nm would result in an unfeasible number of sample points and computation time.

In the remainder of this paper, we introduce our model of FP etalons made of interfaces with spatially varying surface topography illuminated with arbitrary beams. We then validate this new model against PSTD simulations and study its range of validity. Finally, we present exemplar applications including the computation of an ITF for a FP etalon with rough interfaces, and the computation of changes in the transmissivity due to modulation of the cavity thickness by an ultrasonic plane wave.

2. Model

The model is composed of two principle steps. The first step calculates the fields transmitted and reflected by a single interface with arbitrary surface topography. Then, in the second step, the model iteratively evaluates light propagation back and forth between the multiple interfaces forming the FP etalon. The second step allows for all of the round trips generated inside the FP etalon, and the interference between them, to be computed.

2.1. Fields reflected and transmitted by an interface

We define an interface as the infinitely thin surface separating two layers, with refractive indices n_1 and n_2, as illustrated in Fig. 1. The topographic map is defined as a function $\epsilon(x, y)$ which describes the offset along the z-axis between the non-planar interface and an xy-plane through the interface. The aim of this section is to define the reflection ($\mathcal{R}$) and transmission ($\mathcal{T}$) functions [16] for a single interface. These functions relate the angular spectrum of the fields reflected ($\hat{E}_r$) and transmitted ($\hat{E}_t$) by the interface with the angular spectrum of the illumination field ($\hat{E}_i$), respectively.

Optics EXPRESS

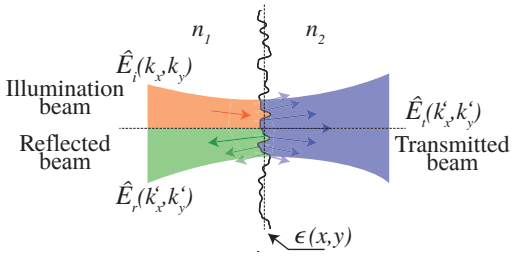

Fig. 1. Schematic of light scattering by an interface with a non-planar surface topography.

2.1.1. Rayleigh-Rice theory

To model a single interface with surface topography the model uses the Rayleigh-Rice theory. This theory calculates the reflected and transmitted fields assuming an incident plane wave with complex amplitude as $\hat{E}_i$ as [17]:

$$\hat{E}_t(k'_x,k'_y) = \begin{cases} \hat{E}_i(k_x,k_y)t_u(k_x,k_y) + \hat{E}_i(k_x,k_y)t_s(k_x,k_y,k'_x,k'_y), & k_x = k'_x \wedge k_y = k'_y \\ \hat{E}_i(k_x,k_y)t_s(k_x,k_y,k'_x,k'_y), & k_x \neq k'_x \vee k_y \neq k'_y \end{cases} \tag{1}$$

$$\hat{E}_r(k'_x,k'_y) = \begin{cases} \hat{E}_i(k_x,k_y)r_u(k_x,k_y) + \hat{E}_i(k_x,k_y)r_s(k_x,k_y,k'_x,k'_y), & k_x = k'_x \wedge k_y = k'_y \\ \hat{E}_i(k_x,k_y)r_s(k_x,k_y,k'_x,k'_y), & k_x \neq k'_x \vee k_y \neq k'_y, \end{cases} \tag{2}$$

where: k_x and k_y are the spatial frequencies of the illumination plane wave; k'_x and k'_y are the spatial frequencies of the reflected and transmitted plane waves; r_u and t_u are the reflection and transmission Fresnel coefficients for a planar dielectric interface; and r_s and t_s are the coefficients relating the illumination and scattered plane wave component amplitudes given by the Rayleigh-Rice theory.

The Rayleigh-Rice theory calculates the coefficients r_s and t_s analytically by assuming that light fields evolve linearly near the interface and that fields are continuous across the interface [17]. The solution is derived by expanding the field into a Taylor series around an xy-plane through the interface and retaining only the zeroth and first order derivative terms. Due to the linearity assumption, this solution is only valid if the magnitude of the topographic map is much smaller than the wavelength in both media forming the interface. The closed-forms expressions of the coefficients r_s and t_s are given as [18,19]:

$$t_s(k_x,k_y,k'_x,k'_y) = -\frac{ik_0^2}{2k_{z2}(k'_x,k'_y)}(n_2^2 - n_1^2)\xi(k'_x - k_x, k'_y - k_y) \\ (1 + r_u(k_x,k_y))(1 - r_u(k'_x,k'_y)), \tag{3}$$

$$r_s(k_x,k_y,k'_x,k'_y) = -\frac{ik_0^2}{2k_{z1}(k'_x,k'_y)}(n_2^2 - n_1^2)\xi(k'_x - k_x, k'_y - k_y) \\ (1 + r_u(k_x,k_y))(1 + r_u(k'_x,k'_y)), \tag{4}$$

where:

$$r_u(k_x,k_y) = \frac{k_{z1}(k_x,k_y) - k_{z2}(k_x,k_y)}{k_{z1}(k_x,k_y) + k_{z2}(k_x,k_y)}; \tag{5}$$

$$t_u(k_x,k_y) = \frac{2k_{z1}(k_x,k_y)}{k_{z1}(k_x,k_y) + k_{z2}(k_x,k_y)}; \tag{6}$$

$$k_z(k_x,k_y) = \sqrt{k^2 - k_x^2 - k_y^2}; \tag{7}$$

Optics EXPRESS

$$\xi(k_x, k_y) = \frac{1}{4\pi} \iint \epsilon(x, y) \exp(i(xk_x + yk_y))dxdy; \tag{8}$$

k_i is the wave number given as $2\pi n_i/\lambda$; n_i is the refractive index of the medium (where i is 1 or 2); λ is the wavelength in a vacuum; and k_0 is the wave number in a vacuum.

2.1.2. Rayleigh-Rice theory for arbitrary fields

The Rayleigh-Rice theory was extended in this paper to treat arbitrary illuminations by combining the angular spectrum formalism with the Rayleigh-Rice theory. In the angular spectrum formalism, an arbitrary field is described as a sum of plane waves propagating with specific complex amplitude and direction of propagation [20]. This formalism allows us to use the Rayleigh-Rice theory to predict how each plane wave component of the incident angular spectrum is reflected and transmitted by an interface [21]. Thus, by applying the Rayleigh-Rice theory to all plane wave components forming the incident angular spectrum, the reflected and transmitted fields can be calculated as:

$$\hat{E}_t(k'_x, k'_y) = \mathcal{T}\hat{E}_i(k_x, k_y) = \hat{E}_i(k'_x, k'_y)t_u(k'_x, k'_y) + \iint \hat{E}_i(k_x, k_y)t_s(k_x, k_y, k'_x, k'_y)dk_xdk_y, \tag{9}$$

$$\hat{E}_r(k'_x, k'_y) = \mathcal{R}\hat{E}_i(k_x, k_y) = \hat{E}_i(k'_x, k'_y)r_u(k'_x, k'_y) + \iint \hat{E}_i(k_x, k_y)r_s(k_x, k_y, k'_x, k'_y)dk_xdk_y, \tag{10}$$

2.1.3. Reducing computational time with fast Fourier transforms

Equations (9) and (10) are relatively time consuming functions to evaluate due them being a convolution. The computational time can be reduced using the convolution theorem to re-write Eqs. (9) and (10) based on the Fast Fourier transform (FFT) as:

$$\begin{aligned}\hat{E}_t(k'_x, k'_y) &= G(k'_x, k'_y) \iint \hat{E}_i(k_x, k_y)H(k_x, k_y)\xi(k'_x - k_x, k'_y - k_y)dk_xdk_y \\ &= G\,\mathcal{F}^{-1}\{\mathcal{F}\{\hat{E}_i\,H\}\,\mathcal{F}\{\xi\}\},\end{aligned} \tag{11}$$

$$\begin{aligned}\hat{E}_r(k'_x, k'_y) &= I(k'_x, k'_y) \iint \hat{E}_i(k_x, k_y)J(k_x, k_y)\xi(k'_x - k_x, k'_y - k_y)dk_xdk_y \\ &= I\,\mathcal{F}^{-1}\{\mathcal{F}\{\hat{E}_i\,J\}\,\mathcal{F}\{\xi\}\},\end{aligned} \tag{12}$$

where:

$$G(k'_x, k'_y) = -\frac{ik_0^2}{2k_{z2}}(n_2^2 - n_1^2)(1 - r_u(k'_x, k'_y)); \tag{13}$$

$$H(k_x, k_y) = (1 + r_u(k_x, k_y)); \tag{14}$$

$$I(k'_x, k'_y) = -\frac{ik_0^2}{2k_{z1}}(n_2^2 - n_1^2)(1 + r_u(k'_x, k'_y)); \tag{15}$$

$$J(k_x, k_y) = (1 + r_u(k_x, k_y)); \tag{16}$$

and $\mathcal{F}$ and $\mathcal{F}^{-1}$ are the fast Fourier and inverse Fourier transforms, respectively.

2.2. Fields reflected and transmitted by a series of interfaces

We define a dielectric stack as a succession of A−1 different layers, each with refractive index n_a and thickness h_a, where the surface topography of each interface is given by a topographic map ϵ_a, as depicted in Fig. 2(a). To calculate the fields transmitted and reflected by the dielectric stack, light must be propagated throughout the entire structure in a manner that considers all of the paths that light can take within the dielectric stack.

Optics EXPRESS

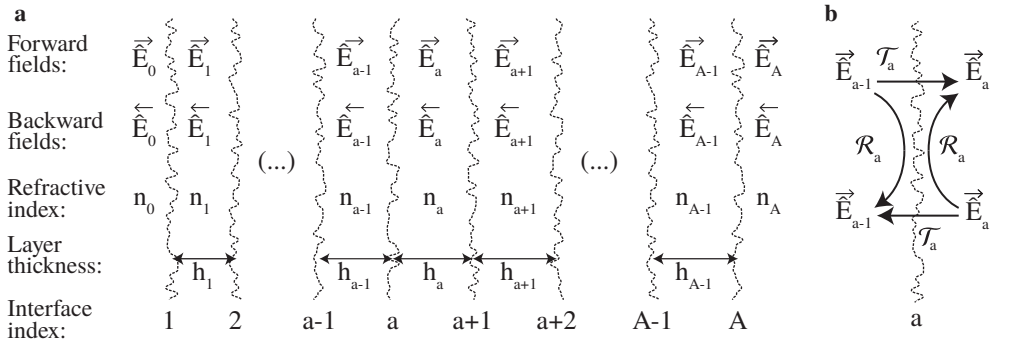

Fig. 2. a) Schematic of all sections of a dielectric stack with interfaces and nomenclature. b) Schematic of the fields transformation in one iteration.

We proceed by dividing the dielectric stack into sections with boundaries defined by each interface, as illustrated in Fig. 2(a). In each section a, the fields propagating backward ($\overleftarrow{\hat{E}}_a$) and forward ($\overrightarrow{\hat{E}}_a$) are stored as a function of (k_x, k_y). In the first model iteration, all fields inside each layer are null, excluding the field incident upon the structure ($\overrightarrow{\hat{E}}_0$), which is the illumination field.

The algorithm progresses by iteratively calculating the contribution to the field in a particular section due to the fields originating from interfaces connected to that section. In particular, at each iteration, the field $\overrightarrow{\hat{E}}_{a-1}$ incident upon the interface a contributes to the field $\overrightarrow{\hat{E}}_a$ upon transmission, whilst the reflected field contributes to $\overleftarrow{\hat{E}}_{a-1}$ upon reflection, as shown in Fig. 2(b). Thus, the iterative algorithm progresses as:

$$\overrightarrow{\hat{E}}_a = \mathcal{T}_a(\overrightarrow{\hat{E}'}_{a-1}\exp(ih_{a-1}\sqrt{k_{a-1}^2 - k_x^2 - k_y^2})) + \mathcal{R}_a(\overleftarrow{\hat{E}'}_a\exp(ih_a\sqrt{k_a^2 - k_x^2 - k_y^2})) \tag{17}$$

$$\overleftarrow{\hat{E}}_a = \mathcal{T}_a(\overleftarrow{\hat{E}'}_{a+1}\exp(ih_{a+1}\sqrt{k_{a+1}^2 - k_x^2 - k_y^2})) + \mathcal{R}_a(\overrightarrow{\hat{E}'}_a\exp(ih_a\sqrt{k_a^2 - k_x^2 - k_y^2})) \tag{18}$$

where the prime symbol $'$ refers to the beams in the previous iteration, $\mathcal{T}_a$ and $\mathcal{R}_a$ are the reflection and transmission functions of the interface a and the exponential term accounts for beam propagation inside the layers. By iteratively evaluating this algorithm until the field intensity inside all of the internal sections (from 1 to A−1) is close to null, the fields reflected ($\overleftarrow{E_0}$) and transmitted ($\overrightarrow{E_A}$) by the dielectric stack are calculated. This algorithm calculates the fields after each round trip of the multi-layered system as is commonly used to model multi-cavity FP etalons [22]. However, this algorithm uses the associative property of the reflection and transmission functions (i.e. $\mathcal{T}_1\mathcal{T}_2\mathcal{R}_3\mathcal{T}_2\overrightarrow{\hat{E}_1} + \mathcal{T}_1\mathcal{R}_2\overrightarrow{\hat{E}_1} = \mathcal{T}_1(\mathcal{T}_2\mathcal{R}_3\mathcal{T}_2\overrightarrow{\hat{E}_1} + \mathcal{R}_2\overrightarrow{\hat{E}_1})$) to reduce the model computational time and memory requirement.

The model uses a scalar field representation and thus neglects the polarization of light. However, a vectorial version of our model could be developed assuming the vectorial properties of light [18–20]. Since FP etalons are typically illuminated with low numerical aperture (NA) beams, the scalar approximation is accurate and the vectorial proprieties can be neglected. Considering also that a vectorial model would take considerably longer to compute, we decided to employ a scalar representation for our model.

Optics EXPRESS

2.3. Model validation

We validated the model by simulating an optical structure which operates as a transparent dielectric stack if the interfaces are planar. This structure, labelled as A, is shown in Fig. 3(a) and is nearly transparent at a wavelength of 1550 nm, because the optical thickness of its layers is half of the wavelength. Structure B is similar to structure A but its layers in the upper half have different thicknesses, as illustrated in Fig. 3(b). Thus, the transmissivity of structure B varies locally due to the change in the thickness of its layers.

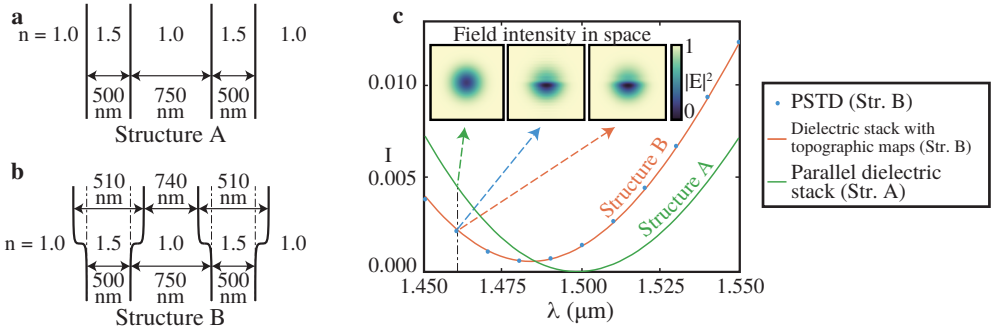

Fig. 3. Comparison of predictions from the dielectric stack model and PSTD simulations. a) Schematic of the structure with planar interfaces. b) Schematic of the structure formed by interfaces with a non-planar topography. For both structures, an illumination Gaussian beam with beam waist of 10 μm was assumed. c) Wavelength resolved reflectivity of structures A and B. The colormaps inside the graph show the beams intensity in space over a 30 μm×30 μm region predicted by the different models.

The wavelength resolved reflectivities of structures A and B were computed to validate the model presented in this paper. Both simulations used a sampling of k_x and k_y from $-0.68k_0$ to $0.70k_0$ with a step size of $0.022k_0$ (64 points). The convergence of the iterative algorithm was considered to be achieved when light intensity inside the internal layers was less than 10^{-6} of the illumination beam intensity. For the structure B, the topographic map of the interfaces was given as:

$$\epsilon(x, y) = (-1)^a \, 5 \left(\frac{\arctan(-x \times 10^{-2})}{\pi} + 0.5 \right) \text{ nm}, \tag{19}$$

where x is in nanometers and a is the interface number. The simulation time was around 0.1 s per wavelength for both structures.

For reference, structure B was also simulated using the PSTD method [23]. In a PSTD simulation, an arbitrary refractive index distribution is discretised into voxels (typically called a Yee cell) to solve Maxwell's equations for the fields reflected and transmitted by the structure. To simulate the structure B, the structure was discretised into voxels with size 1.86 μm × 3.75 μm × 0.005 μm resulting in a total grid of size 160 × 80 × 310 voxels. For the voxels intersecting an interface, the refractive index of the voxel was set by the average refractive index, weighted by the proportion of each material occupying the voxel. The 11 wavelength points were computed in approximately 5 days using a single broadband PSTD simulation [23].

Wavelength resolved reflectivities of both structures computed using both models are plotted in Fig. 3(c). The reflectivity was computed by integrating the intensity of the reflected beam as:

$$I \propto \frac{\int_{-\infty}^{\infty} \int_{-\infty}^{\infty} \left| \hat{E}_r(k_x, k_y) \right|^2 \, dk_x dk_y}{\int_{-\infty}^{\infty} \int_{-\infty}^{\infty} \left| \hat{E}_i(k_x, k_y) \right|^2 \, dk_x dk_y}, \tag{20}$$

Optics EXPRESS

where $\hat{E}_i$ is the beam illuminating the structure and $\hat{E}_r$ is the beam reflected by the structure. The denominator is used for normalisation. The predictions from both models are in agreement for the reflectivity of structure B and differ considerably from the reflectivity of structure A. Thus, based on these simulation, the model presented in this paper is able to account for the impact of variations in the surface topography of the interfaces forming a dielectric stack.

3. Range of validity

This section explores the validity of the FP etalon model. The model is based on the Rayleigh-Rice theory which is know to be valid to model interfaces with surface topography with magnitude much smaller than the optical wavelength. Thus, it is expected that the FP etalon model will be valid in the same circumstances, and that the model accuracy reduces as the height of the surface topography increases [24]. This occurs because, to model interfaces with arbitrary surface topography, the Rayleigh-Rice theory assumes the field to evolve linearly between the xy-plane of the interface and the surface topographic map. As the accuracy of the field linearization decreases with the surface topography, the range of validity was studied as the surface topography increases.

To explore the model range of validity, ITFs predicted by the model were compared against a well-validated reference method. This would ideally be done for a range of different surface topographies. However, there is currently no reference method able to predict the ITFs from FP etalons with arbitrary surface topography. We overcame this challenged by testing the model using a subset of possible surface topographies for which the ground truth can be computed. In particular, we simulated FP etalons in which the topographic map had the same value across x and y (i.e. $\epsilon(x, y) = C$). While the objective of this model is to simulate FP etalon with non-planar surface topography, constant surface topographies were used to change the thickness of the layers forming the FP etalon. Even when simulating constant surface topographies, the field linearization between the xy-plane of the interface and the topographic map occurs meaning that the predictions are impacted by the range of validity of the Rayleigh-Rice theory. Thus, an indication of the model's range of validity was created by comparing simulations of FP etalons with constant topographic maps ($\epsilon(x, y) = C$) against FP etalons without topographic maps ($\epsilon(x, y) = 0$).

The range of validity study was performed by simulating an FP etalon formed by two dielectric mirrors separated by a quartz cavity, illuminated by a Gaussian beam with waist (ω) of 70 µm (full width at $1/\exp(2)$ of the intensity profile). The mirrors of the FP etalon were formed by five di-layers of sodium hexafluoroaluminate (Na_3AlF_6) and zinc sulfide (ZnS) with nominal optical thickness of $\lambda_{des}/4$ where λ_{des}, the design wavelength of the mirror, was 1500 nm. This mirror design has a reflectivity of 98% at 1550 nm. The ground truth was computed with an traditional planar FP etalon model [10], by simulating an FP etalon with cavity thickness 100 µm, as schematised in Fig. 4(a). To quantify the model accuracy as the constant topographic map increases, a range of FP etalons with cavity thicknesses of 100 µm$-C$ were simulated. In the latter case, all layers forming the second mirror of the FP etalon had a topography map of $\epsilon(x, y) = C$, resulting in a total cavity thickness (when accounting with the topographic map) of 100 µm, as illustrated in Fig. 4(b). ITFs with C varying from −15 nm to 15 nm were computed and plotted in Fig. 4(c) along with the ground truth.

As expected, as C increases, the ITFs calculated using our model differ more strongly from the ground truth. For the range considered, the maximum transmissivity of ITFs calculated using the our model tends to increase, relative to the ground truth, by a scaling factor that depends on the magnitude of C. To aid analysis, a scaling error α was defined as:

$$\alpha = \frac{\max(\mathrm{ITF}_1)}{\max(\mathrm{ITF}_2)}, \tag{21}$$

Optics EXPRESS

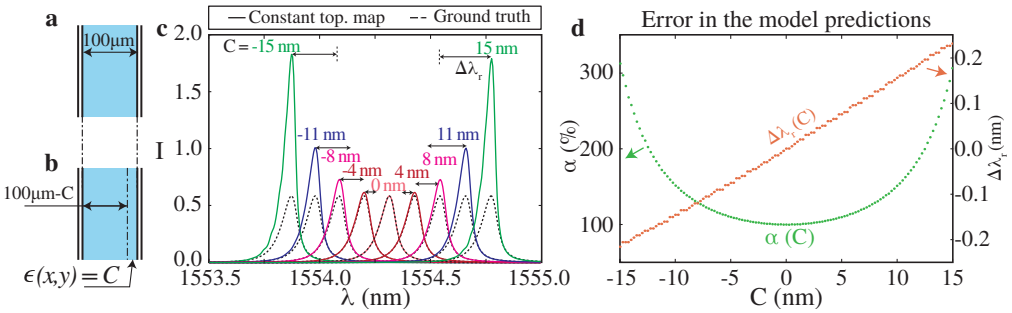

Fig. 4. a-b) Schematic of the FP etalons simulated constant and zero topographic maps. c) Transmissivity plot showing ITFs computed by simulating FP etalon with constant topographic maps along with the ground truth. The ground truth ITFs were shifted according to the horizontal arrows to align with the ITFs predicted by the simulation that accounted for a constant topographic map. d) Scaling error between the maximum transmissivities (α) and difference between the wavelength with maximum transmissivity ($\Delta\lambda_r$) as a function of C.

where ITF_1 and ITF_2 correspond to the ITF from FP etalons with constant non-zero and zero topographic maps, respectively. The scaling error was computed as a function of C and is plotted in Fig. 4(d). As expected, the scaling error is minimum when C is close to zero and increases up to 300% when C is approximately 15 nm. For values of C up to 5 nm, the scaling error is approximately 110%, but rapidly increases to around 150% for values of C around 10 nm. For values of C above 10 nm, α increases more rapidly with increasing C, implying that the model is grossly inaccurate in this region. The increase in the peak intensity of the ITF as C increases is because energy conservation is violated due to the field linearization approximation.

The Rayleigh-Rice approximation also calculates resonant wavelengths inaccurately, as depicted by the horizontal arrows shown in Fig. 4(c). A metric describing the difference between the resonant wavelengths calculated using the two models was defined as:

$$\Delta\lambda_r = \text{argmax}_\lambda(\text{ITF}_1) - \text{argmax}_\lambda(\text{ITF}_2), \tag{22}$$

The difference in the resonance wavelengths was computed and plotted in Fig. 4(d). As is visible in Fig. 4(d), within the range of C considered, the accuracy of the resonant wavelength is linearly dependent on C. The plot in Fig. 4(d) shows that the resonant wavelength predicted is inaccurate by 0.08 nm, 0.15 nm, and 0.23 nm for values of C around 5 nm, 10 nm, and 15 nm, respectively.

The errors presented are only indicative of the accuracy of Rayleigh-Rice theory since simulation of FP etalons with spatially varying topographic maps (the intended application of this model) were not considered. Additionally, the errors determined in this section depend on the specific FP etalon simulated. For example, reducing the mirror reflectivities of the FP etalon would increase the model accuracy. This is because, as the mirror reflectivities decrease, the number of round trips to be computed also decreases, leading to an overall reduction in accumulated error.

4. Example applications

4.1. Rough Fabry-Perot etalon

Two examples were considered to exemplify application of the model. In the first example application, we used the model to predict the ITF from FP etalons in which the surface topography of its interfaces exhibit roughness, as illustrated in Fig. 5(a). For comparison, the ITFs for the same FP etalon, but without roughness, were computed.

Optics EXPRESS

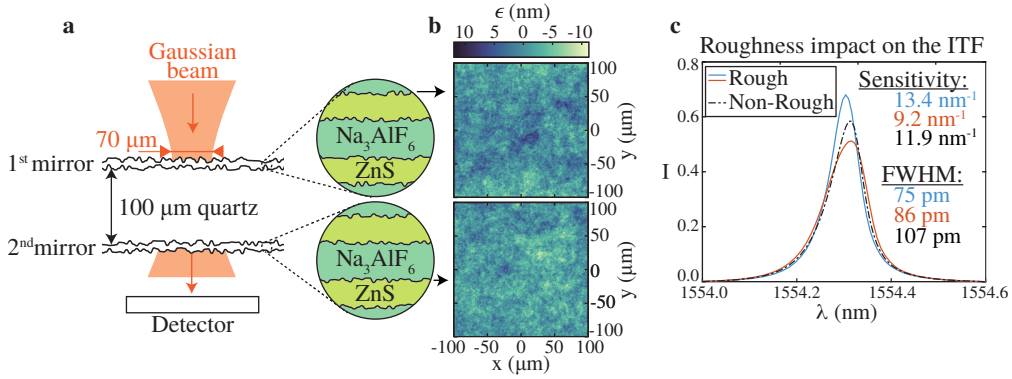

Fig. 5. a) Schematic illustrating the FP etalon with rough interfaces. The design of the FP etalon is the same as in section 3 b) Topographic maps of two interfaces. The Gaussian illumination beam was centred at the point (0 μm, 0 μm). c) Example ITFs computed for an FP etalon with rough mirrors, along with the ITF of the ideal FP etalon with non-rough mirrors. The sensitivity values were computed based on the maximum absolute derivative of the ITF.

The topographic maps were generated computationally using a Fourier based method. In particular, the amplitude of the spectral components of the topographic map were assumed to be given by an ABC model [25]:

$$\hat{\epsilon}(k_x, k_y) = \sqrt{\frac{6 \times 10^8}{\left(1 + 1.23 \times 10^8 \sqrt{k_x^2 + k_y^2}\right)^{-1}}} \text{ nm}. \tag{23}$$

Then, the phase of each spectral component was randomized allowing the topographic map to be calculated using the inverse Fourier transform. The phase randomization was restricted such that the complex amplitude of the spectral components was an even symmetric function (i.e. $\hat{\epsilon}(k_x, k_y) = \overline{\hat{\epsilon}}(-k_x, -k_y)$) leading to a real valued topographic map. The topographic maps of all interfaces were assumed to be uncorrelated, as shown in Fig. 5(b). The RMS of the topographic maps was around 2.69 nm. To maximise the model accuracy, the topographic map generated was imported into the model with a mean of 0 nm. From section 3, the scaling error α for a constant offset of 2.69 nm has a value of 103%, which serves as a indication of the model accuracy. Two ITFs were calculated by simulating two FP etalons, each with independently generated roughness maps.

The computed ITFs are plotted in Fig. 5(c), along with the ITF of the non-rough FP etalon. The resonance wavelength for these simulations is accurately predicted because the mean of the topographic maps is 0 nm. The plots in Fig. 5(c) show that roughness can affect the ITF in a variety of ways. One of the ITFs associated with a rough FP etalon has an increased transmissivity peak and a decreased Full width half maximum (FWHM), relative to the non-rough FP etalon. The opposite behaviour is seen in the other rough FP etalon simulation where the transmissivity peak decreases and the FWHM increases.

The ITFs plotted in Fig. 5(c) do not allow us to draw conclusions regarding the impact of roughness on the FP etalon performance. There are two reasons for this. Firstly, the roughness profiles were randomly generated, but since a statistical study was not performed, the results are not statistically significant. Secondly, we have not investigated whether the topographic maps used accurately represent the roughness found in actual FP etalons. To draw conclusions about

Optics EXPRESS

the impact of roughness, a more in-depth study is required which is beyond the scope of this paper.

4.2. Modulation of the cavity thickness by an ultrasonic wave

In this second example, the model is used to predict the changes in the transmissivity as the cavity thickness is modulated by an ultrasonic plane wave. The topographic map of the layers forming the FP etalon follows the sinusoidal profile of the pressure wave which expands/compresses the cavity locally, as depicted in Fig. 6(a). The simulation protocol emulates the experimental protocol typically used to measure ultrasonic waves with an FP etalon [5]. In particular, the ITF from the FP etalon with an unmodulated cavity was calculated to find the wavelength (λ_b) at which the magnitude of ITF's derivative is maximised, as plotted in Fig. 6(b). Then, the transmissivity at λ_b was computed as the cavity was modulated by the ultrasonic wave.

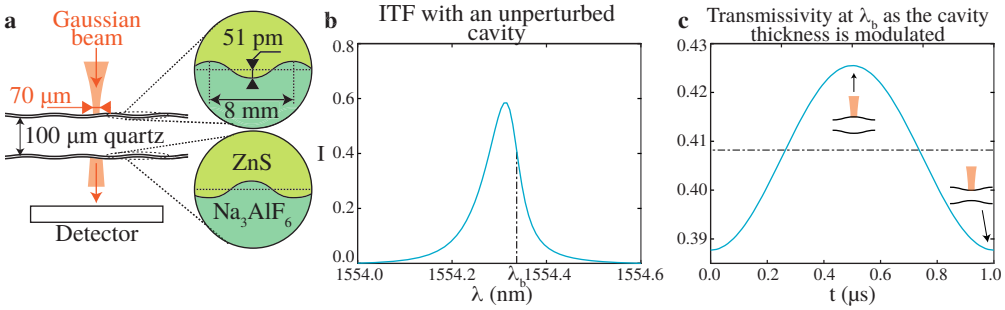

Fig. 6. a) Schematic representing the cavity thickness modulation by an ultrasonic plane wave incident upon the FP etalon. b) ITF of the FP etalon with the cavity thickness unmodulated. c) Variations in the transmissivity at the bias wavelength as the cavity thickness is modulated by the ultrasonic plane wave. The inset illustrations represent the FP etalon cavity modulation for a given moment in time.

The cavity modulation was predicted using a simple mechanical model. In particular, the modulation of the cavity thickness was predicted based on the mechanical properties of the material forming the FP cavity and the properties of the ultrasonic wave. The topographic map of all layers forming the first mirror were given as:

$$\epsilon(x,y) = \frac{Ph}{2\gamma}\cos\left(2\pi\frac{\cos\theta_u f_u x}{v} + 2\pi f_u t\right) + m, \tag{24}$$

and forming the second mirror as:

$$\epsilon(x,y) = -\frac{Ph}{2\gamma}\cos\left(\frac{\cos\theta_u f_u x}{v} + 2\pi f_u t\right) - m, \tag{25}$$

where: θ_u is the polar direction of propagation of the ultrasonic wave inside the FP cavity; f_u is the ultrasonic frequency; γ is the Young's modulus of the material forming the cavity; v is the ultrasonic speed inside the cavity; h is the cavity thickness; P is the peak pressure of the ultrasonic wave; and t is time. The constant m is used to reduce the RMS of the topographic map along the extent of the illumination beam to increase the model accuracy and was calculated as:

$$m = \frac{\iint \frac{Ph\gamma}{2}\cos\left(2\pi\frac{\cos\theta_u f_u x}{v} + 2\pi f_u t\right)\exp\left(-4\frac{x^2+y^2}{\omega^2}\right)dxdy}{\iint \exp\left(-4\frac{x^2+y^2}{\omega^2}\right)dxdy} \tag{26}$$

where ω is the Gaussian beam waist. The constant m did not change the geometry simulated as the cavity thickness was reduced by $2m$ (similarly to as in section 3.).

Optics EXPRESS

As an example, the modulation of the cavity by a 100 kPa ultrasonic wave with frequency of 1 MHz propagating inside the cavity at an angle of 45° was considered. Using the Young's modulus of quartz (97.2 GPa) and a cavity thickness of 100 µm, the peak modulation of each mirror was 51 pm, as illustrated in Fig. 6(a). The modulation of the transmissivity by the ultrasonic wave was computed and plotted in Fig. 6(c) as a function of time. Due to the cavity modulation, the transmissivity is modulated sinusoidally according to the profile of the ultrasonic wave, as expected. For the simulation conditions considered, the constant m reduced the RMS along the beam extent of the topographic map to values below 3.1 pm (instead of 51 pm) resulting in a very accurate set of simulations.

This relatively simple example could be extended to perform more in depth studies. For example, an ultrasonic frequency and directivity study could be performed by computing this example as a function of the ultrasonic frequency and angle of propagation [26,27]. This is particularly interesting as multiple illumination beams could be considered, such as Gaussian [12], Bessel [28], or wavefront-shaped beams [29]. Additionally, more complex models of the cavity modulation could be incorporated into the simulation. Examples include using acoustic models [30] to calculate the cavity thickness map, which would serve as an input to the optics model presented in this paper. However, this optical model cannot account for the localized modulation of the cavity refractive index which might be limiting for some simulations [31]. Similar approaches could be used for modelling different perturbations such as cavity thickness modulation by a temperature change.

5. Conclusion

An extension of Rayleigh-Rice theory to model arbitrary optical beam propagation in a dielectric stack formed of interfaces with non-planar surface topography was presented. The model was validated against PSTD simulations by comparing wavelength resolved reflectivity simulations. As the model is based on the Rayleigh-Rice theory, the model accuracy reduces as the RMS of the topographic map increases. Range of validity tests revealed that when simulating topographic maps with RMS of approximately 5 nm, the shape of the ITF was predicted with an error of approximately 9% and the resonant wavelength with an error of 75 pm. We exemplified application of the model by simulating FP etalons with rough mirrors and an FP etalon with the cavity thickness modulated by an ultrasound plane wave.

The general way that the surface topography of the interfaces is described enables a wide range of potential applications of the model which include: (i) quantifying the impact of rough mirrors on the ITF of FP etalons, (ii) studying the sensing element size of the FP etalon when used for spatially resolved sensing with various illumination beams, and (iii) simulating FP etalons with nearly uniform layered structures, such as micro-resonators [32]. However, the narrow range of validity of the model limits its application and compromises its accuracy. Future work could be aimed at developing a similar model using the generalized Harvey-Shack theory [33]. This theory, as with the Rayleigh-Rice theory, was used to predict the impact of interfaces with non-planar surface topography and has the advantage over the Rayleigh-Rice theory of having a higher range of validity, whilst, however, taking longer to compute [24].

To increase model applicability further, the model was implemented in Jolab, a free and open-source library of optical models able to simulate complex optical systems [34]. This implementation can easily be combined with other models from Jolab to simulate complex optical systems such as rough fibre FP etalons [35], rough FP etalons illuminated through a multi-mode fibre [36], and rough FP etalons illuminated with a wavefront shaped beam [29].

Funding. European Research Council (741149); Engineering and Physical Sciences Research Council (EP/L016478/1); Royal Society (URF\R\191036, URF\R1\180435).

Acknowledgments. The authors acknowledge the use of the UCL Myriad High Performance Computing Facility (Myriad@UCL), and associated support services, in the completion of this work.

Optics EXPRESS

Disclosures. The authors declare no conflicts of interest.

Data availability. The simulated data and code are open-source and available in Code 1, (Ref. [37]).

References

1. A. Perot and C. Fabry, "On the application of interference phenomena to the solution of various problems of spectroscopy and metrology," The Astrophys. J. **9**, 87 (1899).
2. S. R. Mallinson, "Wavelength-selective filters for single-mode fiber WDM systems using Fabry-Perot interferometers," Appl. Opt. **26**(3), 430–436 (1987).
3. E. Martin, E. Z. Zhang, J. A. Guggenheim, P. C. Beard, and B. E. Treeby, "Rapid Spatial Mapping of Focused Ultrasound Fields Using a Planar Fabry-Pérot Sensor," IEEE Trans. Ultrason., Ferroelect., Freq. Contr. **64**(11), 1711–1722 (2017).
4. K. Pham, S. Noimark, N. Huynh, E. Zhang, F. Kuklis, J. Jaros, A. Desjardins, B. Cox, and P. Beard, "Broadband all-optical plane-wave ultrasound imaging system based on a Fabry-Perot scanner," IEEE Trans. Ultrason., Ferroelect., Freq. Contr. **68**(4), 1007–1016 (2021).
5. P. Beard, F. Perennes, and T. Mills, "Transduction mechanisms of the Fabry-Perot polymer film sensing concept for wideband ultrasound detection," IEEE Transactions on Ultrasonics, Ferroelectrics and Frequency Control **46**(6), 1575–1582 (1999).
6. M. Vaughan, *The Fabry-Perot interferometer: history, theory, practice and applications* (Routledge, 2017).
7. E. Nichelatti and G. Salvetti, "Spatial and spectral response of a Fabry-Perot interferometer illuminated by a Gaussian beam," Appl. Opt. **34**(22), 4703 (1995).
8. J. Y. Lee, J. W. Hahn, and H.-W. Lee, "Spatiospectral transmission of a plane-mirror Fabry-Perot interferometer with nonuniform finite-size diffraction beam illuminations," J. Opt. Soc. Am. A **19**(5), 973 (2002).
9. D. M. Marques, J. A. Guggenheim, and P. R. T. Munro, "Angular Airy function: a model of Fabry-Perot etalons illuminated by arbitrary beams," Opt. Express **29**(15), 24144 (2021).
10. D. M. Marques, J. A. Guggenheim, R. Ansari, E. Z. Zhang, P. C. Beard, and P. R. T. Munro, "Modelling Fabry-Pérot etalons illuminated by focussed beams," Opt. Express **28**(5), 7691 (2020).
11. A. J. Cox and D. C. Dibble, "Nondiffracting beam from a spatially filtered Fabry–Perot resonator," J. Opt. Soc. Am. A **9**(2), 282 (1992).
12. E. Zhang, J. Laufer, and P. Beard, "Backward-mode multiwavelength photoacoustic scanner using a planar Fabry-Perot polymer film ultrasound sensor for high-resolution three-dimensional imaging of biological tissues," Appl. Opt. **47**(4), 561 (2008).
13. K. Tan, H. Zhang, M. Wen, and Z. Du, "Effects of the film thickness on the morphology, structure, and crystal orientation behavior of poly(chloro-p-xylylene) Films," J. Appl. Polym. Sci. 132, n/a (2015).
14. A. Taflove, S. C. Hagness, and M. Piket-May, "Computational electromagnetics: the finite-difference time-domain method," The Electr. Eng. Handb. **3**, 629–670 (2005).
15. Q. H. Liu, "The PSTD algorithm: A time-domain method requiring only two cells per wavelength," Microw. Opt. Technol. Lett. **15**(3), 158–165 (1997).
16. R. Shi, N. Janunts, C. Hellmann, and F. Wyrowski, "Vectorial physical-optics modeling of Fourier microscopy systems in nanooptics," J. Opt. Soc. Am. A **37**(7), 1193 (2020).
17. J. M. Elson, "Multilayer-coated optics: guided-wave coupling and scattering by means of interface random roughness," J. Opt. Soc. Am. A **12**(4), 729 (1995).
18. P. Imperatore, A. Iodice, and D. Riccio, "Electromagnetic wave scattering from layered structures with an arbitrary number of rough interfaces," IEEE Trans. Geosci. Remote Sensing **47**(4), 1056–1072 (2009).
19. P. Imperatore, A. Iodice, and D. Riccio, "Transmission through layered media with rough boundaries: First-order perturbative solution," IEEE Trans. Antennas Propag. **57**(5), 1481–1494 (2009).
20. L. Novotny and B. Hecht, *Principles of nano-optics* (Cambridge University, 2012).
21. P. Török, P. D. Higdon, R. Juškaitis, and T. Wilson, "Optimising the image contrast of conventional and confocal optical microscopes imaging finite sized spherical gold scatterers," Opt. Commun. **155**(4-6), 335–341 (1998).
22. D. M. Marques, J. A. Guggenheim, and P. R. T. Munro, "Analysing the impact of non-parallelism in Fabry-Perot etalons through optical modelling," Opt. Express **29**(14), 21603 (2021).
23. P. R. T. Munro, D. Engelke, and D. D. Sampson, "A compact source condition for modelling focused fields using the pseudospectral time-domain method," Opt. Express **22**(5), 5599 (2014).
24. S. Schröder, A. Duparré, L. Coriand, A. Tünnermann, D. H. Penalver, and J. E. Harvey, "Modeling of light scattering in different regimes of surface roughness," Opt. Express **19**(10), 9820 (2011).
25. Y. Gong, S. T. Misture, P. Gao, and N. P. Mellott, "Surface roughness measurements using power spectrum density analysis with enhanced spatial correlation length," J. Phys. Chem. C **120**(39), 22358–22364 (2016).
26. B. T. Cox and P. C. Beard, "Frequency dependent directivity of a planar Fabry Perot polymer film ultrasound sensor," IEEE Trans. Ultrason. Ferroelectr. Freq. Control **54**(2), 394–404 (2007).
27. D. R. Ramasawmy, E. Martin, J. A. Guggenheim, E. Z. Zhang, P. C. Beard, B. E. Treeby, and B. T. Cox, "Analysis of the Directivity of Glass-Etalon Fabry–Pérot Ultrasound Sensors," IEEE Trans. Ultrason., Ferroelect., Freq. Contr. **66**(9), 1504–1513 (2019).

Optics EXPRESS

28. O. J. Sheppard, J. A. Guggenheim, D. M. Marques, R. Ansari, E. Z. Zhang, P. C. Beard, and P. R. T. Munro, "Interrogation of Fabry-Pérot ultrasound sensors with Bessel beams," in *Photons Plus Ultrasound: Imaging and Sensing 2020*, A. A. Oraevsky and L. V. Wang, eds. (SPIE, 2020), p. 39.
29. J. Czuchnowski and R. Prevedel, "Adaptive optics enhanced sensitivity in Fabry-Pérot based photoacoustic tomography," Photoacoustics **23**, 100276 (2021).
30. D. R. Ramasawmy, B. T. Cox, and B. E. Treeby, "ElasticMatrix: A MATLAB toolbox for anisotropic elastic wave propagation in layered media," SoftwareX **11**, 100397 (2020).
31. D. R. Ramasawmy, "Modelling the Directional Response of Fabry-Pérot Ultrasound Sensors," Ph.D. thesis, University College London (2020).
32. J. A. Guggenheim, J. Li, T. J. Allen, R. J. Colchester, S. Noimark, O. Ogunlade, I. P. Parkin, I. Papakonstantinou, A. E. Desjardins, E. Z. Zhang, and P. C. Beard, "Ultrasensitive plano-concave optical microresonators for ultrasound sensing," Nat. Photonics **11**(11), 714–719 (2017).
33. J. E. Harvey, A. Krywonos, and J. C. Stover, "Unified scatter model for rough surfaces at large incident and scatter angles," in *Advanced Characterization Techniques for Optics, Semiconductors, and Nanotechnologies III*, A. Duparré, B. Singh, and Z.-H. Gu, eds. (2007), p. 66720C.
34. D. Marques, J. A. Guggenheim, and P. R. T. Munro, "Jolab a free and open-source software to simulate light propagation in optical systems," in *Three-Dimensional and Multidimensional Microscopy: Image Acquisition and Processing XXVIII*, T. G. Brown, T. Wilson, and L. Waller, eds. (SPIE, 2021), p. 38.
35. P. Morris, "A Fabry-Perot fibre-optic hydrophone for the characterisation of ultrasound fields," PhD Thesis, University of London (2008).
36. B. Keenlyside, D. Marques, M. Cherkashin, E. Zhang, P. Munro, P. Beard, and J. Guggenheim, "Wavefront shaping through multimode fibres to enable endoscopic photoacoustic tomography," in *Adaptive Optics and Wavefront Control for Biological Systems VII*, T. G. Bifano, S. Gigan, and N. Ji, eds. (SPIE, 2021), p. 14.
37. D. M. Marques, J. A. Guggenheim, and P. R. T. Munro, "A numerical model of light propagation through Fabry-Perot etalons composed of interfaces with non-planar surface topography," GitHub (2022) [retrieved 15 November 2022], https://github.com/PhotoacousticUoB/Papers.